Module 5: Schlieren and Shadowgraph

Lecture 30: Three dimensional reconstruction of schlieren data

The Lecture Contains:

Previous Next

THREE DIMENSIONAL RECONSTRUCTION FROM SCHLIEREN DATA

The schlieren image yields gradients of refractive index and hence concentration. As discussed in Section Data Reduction, the gradient information can be integrated to yield data in terms of concentration itself. Subsequently, the concentration field on selected horizontal planes above the growing crystal can be reconstructed using principles of tomography.

Here, the left side of Equation 3 (Lecture 26) is interpreted as projection data of the refractive index gradient.

The schlieren images have been utilized to reconstruct the concentration field on horizontal planes above the crystal. For this purpose, images have been recorded at four different view angles. Since these images are time-separated, the present study is restricted to a steady convection conditions. Minor changes in the concentration field with time have been accounted for by averaging a sequence of four successive images. The schlieren images recorded during the initial transients as well as late stages of growth when convection is unsteady have not been utilized for three dimensional reconstruction.

Computed Tomography

Tomography has been used in the present work to reconstruct two-dimensional concentration field over individual horizontal planes from their one-dimensional projections. The third dimension is filled by moving from one plane to the next in the third (vertical) direction. The recording configuration shown in Figure 5.16 is the parallel beam geometry. The convolution back projection (CBP) algorithm has been used in the present study for tomographic reconstruction. Significant advantages of this method include its non-iterative character, availability of analytical results on convergence of the solution with respect to the projection data, and established error estimates.

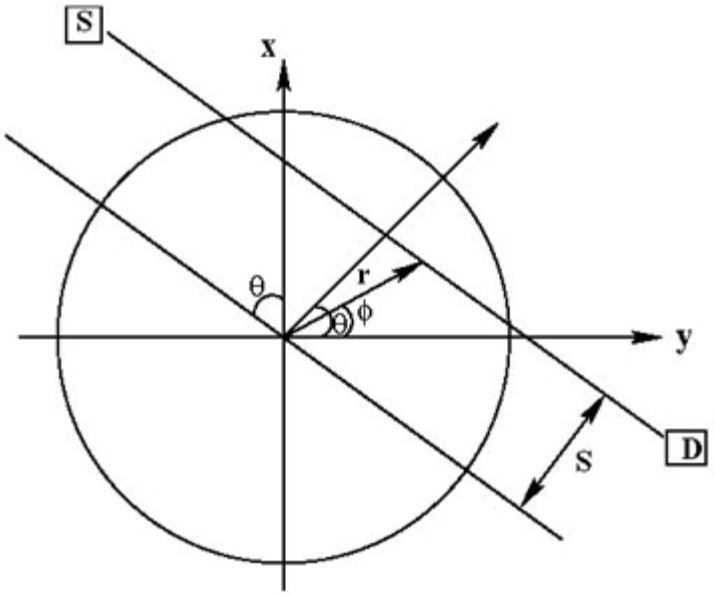

Figure 5.16: Schematic drawing of data collection using parallel beam geometry. S- source, D-Detector, s-perpendicular distance from the center of the object to the ray, θ-view angle, and (r, ϕ)- polar coordinates.

Previous Next

Contd...

In an experiment, projection data can be recorded either by turning the crystal growth chamber or the source-detector combination. The latter is particularly difficult due to stringent requirement of alignment. With the first option, it is not possible to record a large number of projections, owing to the inconvenience of installing plane optical windows in a circular beaker. Further, for a cylindrical growth chamber, the entire field of interest cannot be imaged due to the curvature of the test cell. Instead, the central core region (corresponding to the size of the optical windows), that includes the growing crystal, has been recorded. In this respect, the projection data set is incomplete. In order to generate a complete projection data set for each view angle, an extrapolation procedure has been adopted and is discussed in the next section.

Projection data has been recorded for four view angles of $(0, 45, 90, and\ 135°)$ in the present experiments. The data for 180^0 is taken to be identical to that for zero angle. Information for intermediate view angles has been generated by employing linear interpolation on the experimentally recorded data.

Previous Next

EXTRAPOLATION SCHEME

The experimental set up employed in the present work enables only a part of the aqueous solution in the beaker to be scanned by the laser beam, being limited by the size of the optical windows. The projection data is thus incomplete, as shown schematically in Figure 5.17. Specifically, the experimental data in the form of the schlieren images covers about 25% of the beaker diameter.

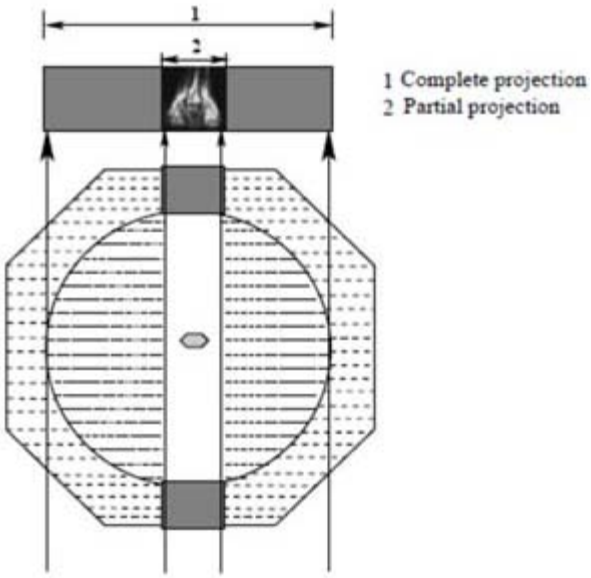

Figure 5.17: Definition of partial projection data.

In order to successfully apply the CBP algorithm for tomographic inversion, one needs projection data over the entire width of the physical domain for each view angle. In the present work, the experimentally recorded partial data has been extrapolated to derive information about the portion of the solution beyond the optical windows. In all experiments, the region inclusive of the crystal has been imaged; extrapolation is applied to the portion of the field from the edges of the laser beam to the walls of the beaker.

Previous Next

The applicability of extrapolation to the present study can be justified on the basis of two factors: First, the concentration level away from the growing crystal, corresponding to the supersaturated solution is practically constant. This is confirmed in the recorded schlieren images where the changes in the intensity are found to be localized in the vicinity of the growing crystal alone. These images are discussed in the subsequent sections. Secondly, the information content of schlieren images decrease with the geometric path length of the light beam within the beaker, as indicated by the integration limits in Equation 3 (Lecture 26). The diminishing chord length of the beaker towards the edges shows that the measurement procedure de-emphasizes concentration variation occurring towards the sides of the beaker. Specifically, the chord length is zero at the extremities of the beaker. The approximation involved in extrapolating concentration outside the measurement volume is thus expected to be less serious in predicting the concentration field closer to the center of the beaker and hence the crystal location. Further justification can be based on the fact that concentration is continuously distributed in the fluid volume.

In the present work, a tenth order polynomial has been used to extrapolate the concentration distribution, starting with the portion covered by the optical windows. Polynomials of order 5 to 10 produced practically identical results. The limiting values of concentration in the far field, and the necessity of maintaining slope-continuity in the concentration distribution at every point have been enforced. An independent check on the accuracy of the experiment, data analysis and extrapolation is the conservation of solutal mass in each of the projections. Mass balance was found to be better than 0.01% in all the experiments analyzed using tomography. Minor imbalances are subsequently rectified by normalizing the data-set. To account for changes in the integration length along the direction of the laser beam, the extrapolated data is multiplied by the local chord length as one proceeds from the center towards the periphery of the growth chamber. This projection data is used for tomographic reconstruction of the concentration field over a horizontal plane of the solution. The above approach has been successfully tested in the context of numerically simulated buoyancy-driven convection and is discussed in the section Validation of Reconstruction Procedure With Simulated Data.

Previous Next

CONVOLUTION BACK-PROJECTION

In the convolution back-projection algorithm (CBP), the reconstructed function, $f(r, \phi)$, is evaluated by the integral formula

$$f(r,\emptyset) = \int_{0}^{\pi} \int_{-D/2}^{D/2} p\big((s' - s);\, \theta\big)\, q(s)\, ds d\theta \qquad (5)$$

where

$$q(s) = \int_{-Re}^{Re} |R|\, W(R) \exp(i2\pi Rs) dR$$

Here $p(s;\theta)$ is the projection data and s is the perpendicular distance of the data ray from the center of the object. In addition, θ denotes the source-detector line with respect to a fixed axis (and hence the view angle), D is the diameter of the growth chamber, and *s*' is the *s*-value of the data ray passing through the point (r, ϕ). The symbol R is the Fourier frequency, $q(s)$ is the convolving function of Equation 5, and $W(R)$ is the filter function. Also see Figure 5.16 for an explanation on the notation used. The filter function vanishes outside the interval $[-R_{c,} + R_c]$ and is an even function of R. Here R_c is the Fourier cut-off frequency and is taken to be $1/2\Delta s, \Delta s$ being the ray spacing. The reconstruction obtained is specific to the choice of the filter function A Hamming filter h 54 has been used in the present study. For $|R| < R_c$ it is given by the formula

$$W(R) = 0.54 + (1 - 0.54) \cos\left(\frac{\pi R}{R_c}\right)$$

This filter emphasizes the smooth features of the concentration variation, while suppressing small-scale (fine structure) fluctuations. This is quite appropriate to the present study for the following reason. Density variations in the solution arise primarily because of the deposition of the solute on the growing faces of the crystal as the solution is cooled at a given rate. Since the crystal growth rate is slow, one encounters density variations that are distributed in the entire solution, while rapid fluctuations in concentration do not appear. Hence, it is of interest to reconstruct the dominant pattern in the concentration field rather than its secondary features.

Previous Next

VALIDATION OF RECONSTRUCTION PROCEDURE WITH SIMULATED DATA

The goal of the present work is to obtain concentration distribution on selected planes above the crystal growing from its aqueous solution from the schlieren images. These images require to be extrapolated to fill the width of the beaker. The extrapolation step combined with the convolution back-projection algorithm is first validated against simulated data. The physical problem considered is buoyancy-driven convection in a differentially heated circular fluid layer with upper and lower walls maintained at specified temperatures. The side wall that is circular is thermally insulated. The fluid considered is air and the Rayleigh number based on the height of the fluid layer is set at $Ra = 12{,}000$. The temperature distribution in the fluid layer has been obtained by numerically solving the governing equations of flow and energy transport on a fine grid. For definiteness, the thermal field is taken to be axisymmetric; accordingly the isotherms on individual planes of the fluid layer are circular.

With the solution for temperature determined numerically, the projection of the thermal field is obtained by path integration. The accuracy of reconstruction with partial data has been examined in the present study against the available numerical solution.

Errors have been reported in the present section on three grids, namely 64 X 64, 128 X 128 and 256 X 256. Here, the first number represents the number of view angles along which projections have been recorded, and the second indicates the number of rays for each view. The definitions of errors considered are:

$$E_1 = \max\left[(T_{orig} - T_{recon})\right]$$ absolute maximum temperature difference

$$E_2 = \sqrt{\frac{1}{N}\sum\left[T_{orig} - T_{recon}\right]^2}$$ RMS error

Here T_{orig} and T_{recon} are the original and reconstructed temperature fields respectively and E_1 and E_2 arises from the fact that the former highlights large isolated errors, while the latter reveals trends that are applicable for the entire cross-section.

Previous Next

The validation of the reconstruction procedure with simulated data is summarized in Figure 5.18.

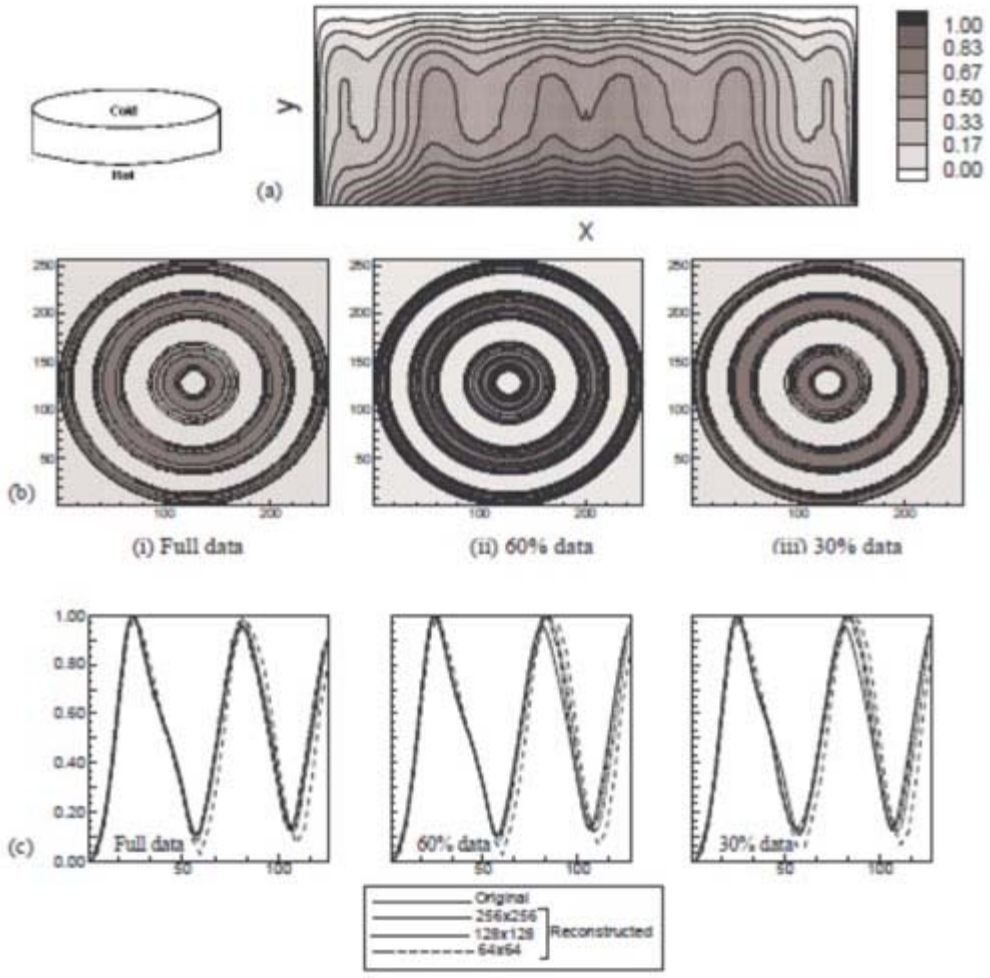

Figure 5.18: Buoyancy-driven convection in a differentially heated circular cavity. (a) Complete projection data in the form of isotherms for the differentially heated circular fluid layer; (b) Reconstructed temperature contours at y/H=0.65 for full (i) 100% and partial (60% (ii), 30% (iii)) projection data; and (c) Comparision of original and reconstructed non-dimensional temperature distribution along the radial direction for the three different combinations of rays and views.

Figure 5.18(a) shows isotherms of the thermal field in the fluid layer for a given view angle. This data is presented in the form of contours of the path integrated temperature field. Since the thermal field is axisymmetric, the projection data for all other view angles are identical to Figure 5.18(a). The reconstruction over a horizontal plane of the fluid layer is shown in Figure 5.18(b).

Previous Next

Results obtained with complete projection data (marked 100% in 5.18b(i)) and partial data (60% in 5.18b(ii) and 30% in 5.18b(iii), symmetrically placed about the center) are also shown. The axisymmetric nature of temperature distribution is brought out in all the reconstructions. This can be taken as a validation of the extrapolation procedure used to convert partial to an approximate but complete data set. A quantitative comparison of the reconstructed temperature profiles along the diameter of the cavity for different combinations of rays and views are shown in Figure 5.18(c). Profiles obtained with full as well as partial data are reported. For the complete data set, a perfect match between the original and reconstructed profiles can be seen for grid sizes of 128 X 128 and 256 X 256, while small errors are to be seen for the 64 X 64 grid. The extent of deviation from the original increases as the fraction of incomplete data increases. Noticeable errors are to be seen when only 30% of the original data is used, the rest of it being derived by extrapolation. Errors in reconstruction were found to be significantly higher when the partial data set was used without extrapolation.

The magnitudes of errors as a function of discretization of the fluid layer and size of the partial data set are summarized in Table 1. Since the difference between the minimum and maximum temperatures is unity, the percentage error is obtained as $100 \times E_1$ *and* $100 \times E_2$.

Table 1: Comparision of the original and reconstructed temperature feilds in terms of errors E_1 and E_2 for buoyancy-driven convection in a circular cavity.

Data Type		Rays X Views	E_1	E_2
Full Data		256 X 256	0.052	0.028
		128 X 128	0.109	0.056
		64 X 64	0.124	0.058
Partial Data	60%	256 X 256	0.095	0.039
		128 X 128	0.148	0.061
		64 X 64	0.152	0.067
	30%	256 X 256	0.122	0.051
		128 X 128	0.148	0.072
		64 X 64	0.173	0.076

. In Table 1, error E_1 is consistently seen to be higher than E_2 the latter being an average over the entire field. Both errors decrease as the grid size (number of rays and views) increases. For a given grid size, errors increase as the fraction of original data used in reconstruction decreases. When only 30% of the original is used (the rest being obtained by extrapolation), the maximum errors on a 64 X 64 grid are 17.3% (absolute maximum) and 7.6% (RMS). Figure 5.18 shows that the corresponding reconstructions are qualitatively meaningful, and hence these error magnitudes may be taken to be within limits.

Previous Next

BENCHMARK EXPERIMENT: A COMPARISON OF INTERFEROMETRY, SCHLIEREN AND SHADOWGRAPH

A direct comparison of images of convection seen in interferometry, schlieren and shadowgraph is presented here. The physical experiment considered is a differentially heated fluid layer enclosed in a rectangular cavity. In the initial discussion, the temperature difference across the cavity is 10 K in the experiments, while the fluid medium in the cavity is air. The corresponding Rayleigh number has been calculated to be 6×10^4 The interferograms, schlieren and shadowgraph images are compared on the right column of Figure 5.19. The fringes of an interferogram are lines of constant temperature. With reference to the discussion in Section Data Reduction, temperature here is to be interpreted as an integrated value over the length of the cavity. It should be noted that fringe shapes in a circular geometry are harder to interpret owing to a change in the geometric path length in a direction the path of the light beam.

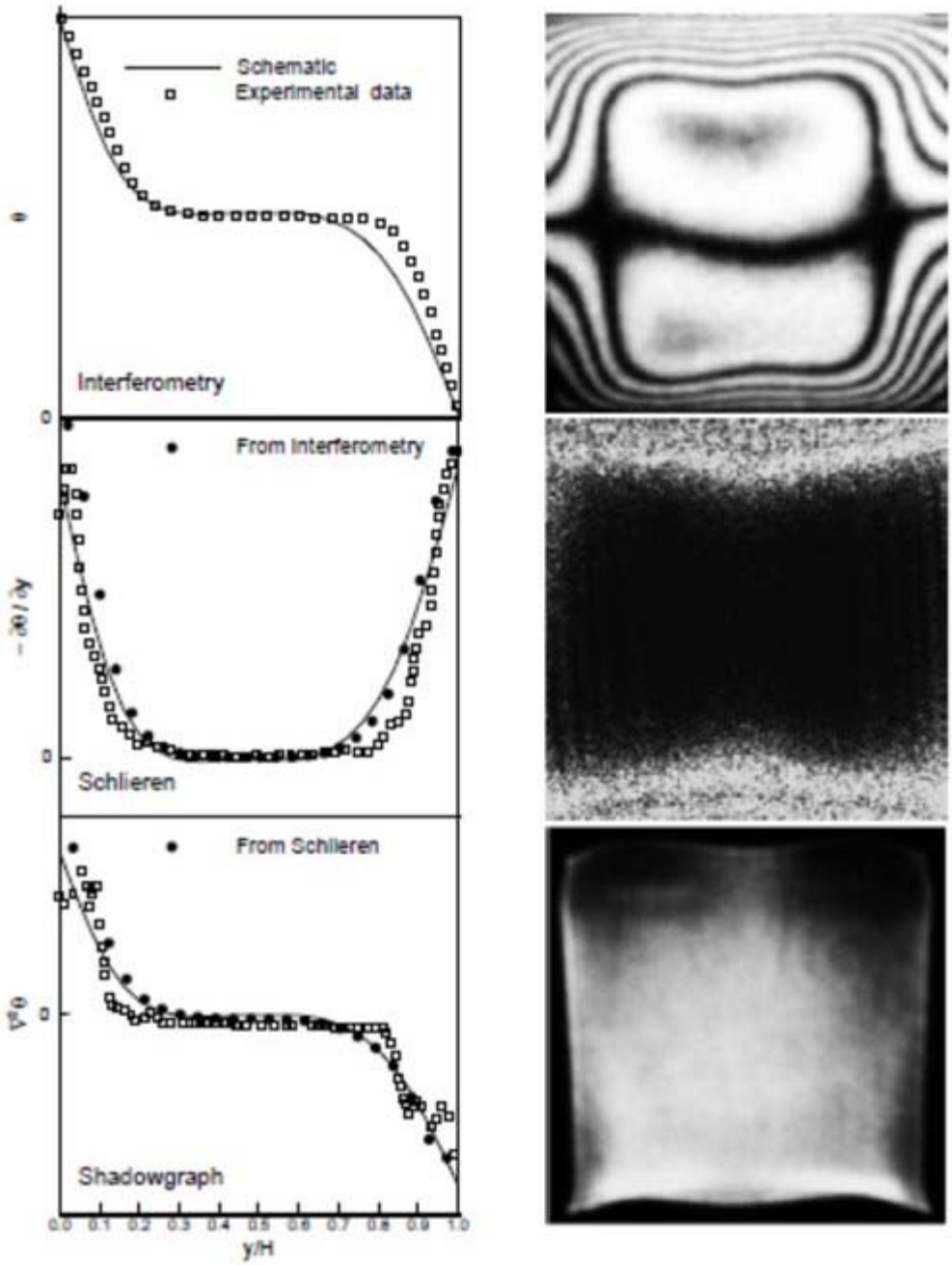

Figure 5.19:Comparision of data recovered from the three optical techniques (left column). The corresponding experimental images are shown in the right column. $Ra = 1.30 \times 10^4$. The solid line in the left column is representative of the trend seen at any vertical section of the image.

Previous Next

The spatial coordinates of the fringes can be used to obtain the temperature profile. For schlieren and shadowgraph, the information regarding the thermal field is contained in the light intensity variation. The respective thermal properties recovered are the local values of the first derivative and the Laplace operator applied to the temperature. These quantities have been plotted for the mid-plane of the cavity on the left side of Figure 5.19. The individual data points are specific to the mid-plane of the cavity, while the solid line indicates the overall trend. The shaded circles of the left column indicate the gradients calculated from interferometric data (for schlieren) and from schlieren data (for shadowgraph). A good overall match is a confirmation of the result that schlieren is a derivative of the interferometric field, and the shadowgraph in turn is the derivative of the schlieren. The appearance of dense fringes near the horizontal walls is indicative of high temperature gradients at these locations. This is brought in the schlieren image in the form of an increase in intensity as well as the data points. The central region is a zone of nearly constant temperature, where the gradients (and the light intensity values) are close to zero. Thus, the schlieren images and interferograms correlate quite well with each other. They also correlate with the shadowgraph, once it is realized that in this approach, light is redistributed over the image. In a shadowgraph image, light from the region close to the cold top wall deflects towards the lower hot wall, where the light intensity shows a maximum. Thus, high gradients are represented in a shadowgraph by regions of very low as well as very high light intensity. In the central core, the change in light intensity with respect to the initial setting is small. Thus the Laplacian operation of temperature in this region yields a practically zero value. The thermal lensing effect that distorts the shape of the cavity cross-section is most visible in the shadowgraph.

Quantitative analysis of the temperature field and wall heat transfer rates is reported for the lower range of cavity temperature differences (and hence Rayleigh number). Clear shadowgraph images could not be recorded for small temperature differences and have not been shown. At higher temperature differences, the field was seen to become unsteady. The discussion for larger cavity temperature differences is based on qualitative comparison of the three imaging techniques.

Previous Next

Low Rayleigh numbers

Figure 5.10 shows the steady state interferometric and schlieren images for the lower range of Rayleigh numbers namely $1.3 \times 10^4 < Ra < 5 \times 10^4$. At $Ra = 1.3 \times 10^4$ the interferogram has only a few fringes. The number of fringes in the experiments was uniformly found to be consistent with the estimate $(T_h - T_c)/\Delta T_c$ the denominator being given by Equation 1 (Lecture 29). The number of fringes increases with Rayleigh number, along with the fringe density near the horizontal walls. With respect to the schlieren images, it can be seen that the increase in light intensity is distributed over the cavity cross-section at the lowest Rayleigh number. As Rayleigh number increases, the brightness is limited to the wall region, and its size progressively diminishes. The schlieren image clearly brings out a boundary-layer type of flow structure in the cavity. The above experiments have been validated against a numerical model and the comparison has been found to be good.

A comparison of the steady dimensionless temperature profiles in the cavity as obtained from interferometry, schlieren, and numerical simulation is presented in Figure 5.21. Temperature profiles at two column locations $(x/h = 1/4 \; and \; 3/4)$ have been considered. The comparison has been presented for the three Rayleigh numbers referred in Figure 5.20. The shape of the temperature profile, characteristic of buoyancy-driven convection in a Rayleigh-Benard configuration is reflected in all the three approaches. The slopes of the individual curves near the walls give a measure of the wall heat flux. The comparison between the experiments and simulation is seen to be good. Schlieren measurements compare marginally better with numerical simulation, as against interferometry. This is because in interferograms, information about the thermal field is available only at the fringes. Constructing a complete temperature profile requires interpolation between fringes, and is a source of error. In addition, the number of fringes at low Rayleigh numbers is small.

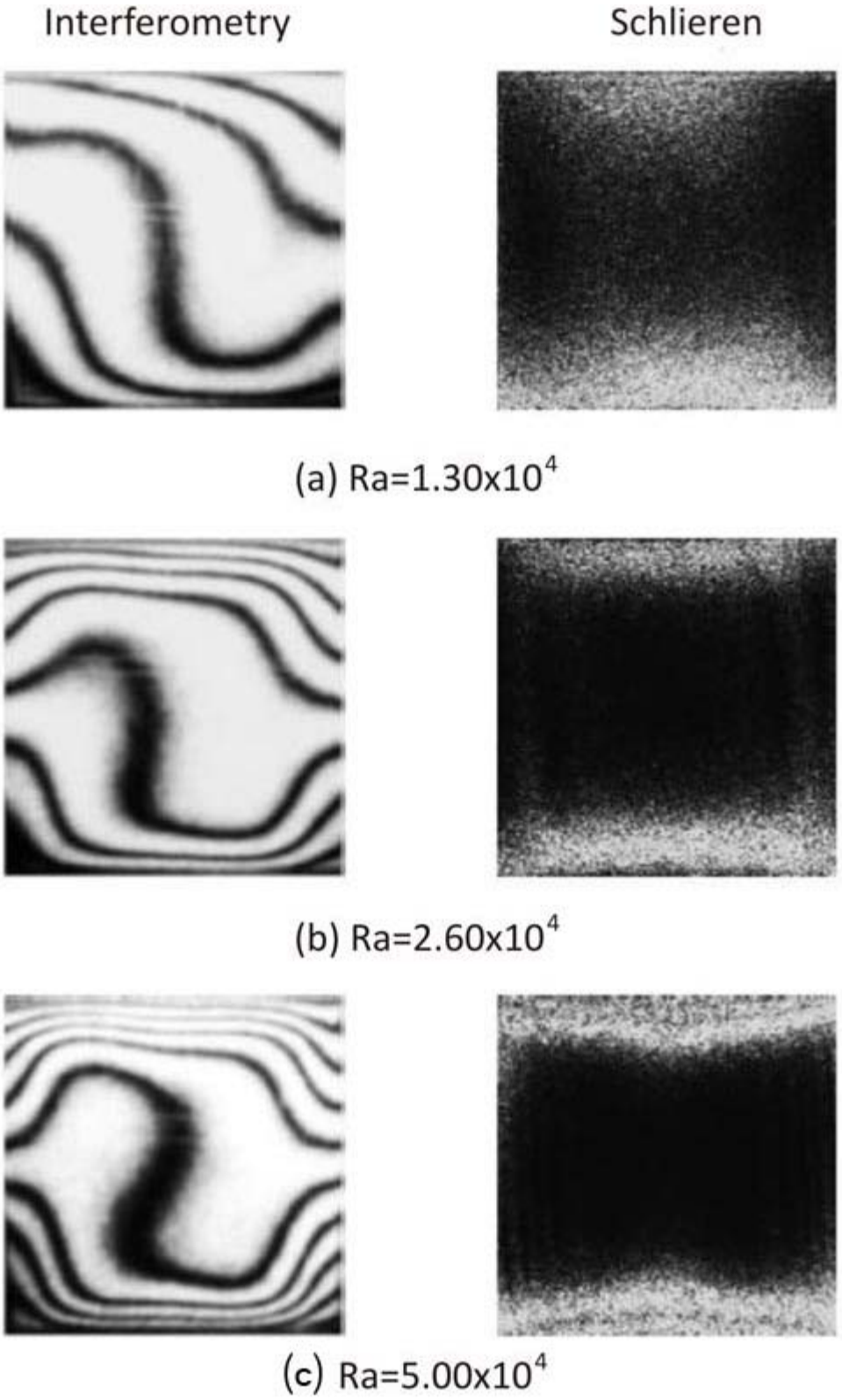

Figure 5.20: Interferometric and schlieren images for the lower range of Rayleigh numbers in air.

Previous Next

Under steady conditions, the average wall heat flux is also equal to the energy transferred across any horizontal plane of the cavity. Average heat transfer rates at the hot and the cold walls of the cavity have been calculated in terms of Nusselt number and presented in Table 2. Further, they have been compared against an experimental correlation. The correlation summarizes the observations of a number of authors and cavity dimensions. Consequently, it has a large uncertainty level of $\pm$20%. The average Nusselt numbers predicted by the two optical techniques match well with each other, with a maximum difference of $\pm$5%, that occurs at the lowest Rayleigh number (Ra= 1.3×10^4) of the present work. The hot and cold wall Nusselt numbers are also reasonably close, indicating a good energy balance in the data reduction procedure. The discrepancies are higher in interferometry at this Rayleigh number owing to the formation of just a few fringes in the cavity.

Table 2: Wall-averaged Nusselt numbers at the lower (hot) and the upper (cold) walls for convection in a rectangular cavity with air as the working fluid. Comparision of experiments with corelation of Gebhart et al (1988). Symbol I in brackets indicates values calculated from interferograms; symbols S indicates values calculated from a schlieren image.

Rayleigh Number	Nu(cold)	Nu(hot)	Nu (Reference)
1.3×10^4	2.38 (I) 2.28 (S)	1.965 (I) 2.07 (S)	2.615
2.6×10^4	3.32 (I) 3.50 (S)	3.13 (I) 3.10 (S)	3.03
5.0×10^4	3.56 (I) 3.37 (S)	3.51 (I) 3.38 (S)	3.45

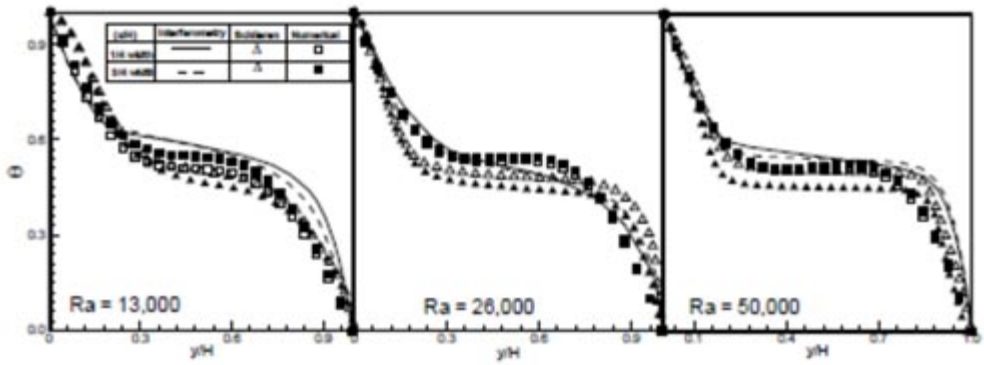

Figure 5.21: Convection in an air-filled cavity. Non-Dimensional temperature profiles as a function of the vertical coordiante.

Previous Next

High Rayleigh numbers

Convection in a cavity subjected to a large temperature difference and hence a high Rayleigh number is discussed in the present section. The shadowgraph images were quite clear in these experiments and have been included for comparison. In each of the experiments, a true steady state was not attained even after the passage of a long period of time. Secondly, interferograms were subjected to large refraction errors. The cavity viewed through the schlieren and shadowgraph layouts looked deformed once again due to refraction. Hence, the present discussion is purely descriptive and quantitative data has not been reported. Rayleigh numbers considered are $Ra = 8.5 \times 10^4, 1.1 \times 10^5 \; and \; 1.4 \times 10^5$.

Figure 5.22 shows representative images of the convective field recorded after the passage of 8-9 hours of real time.

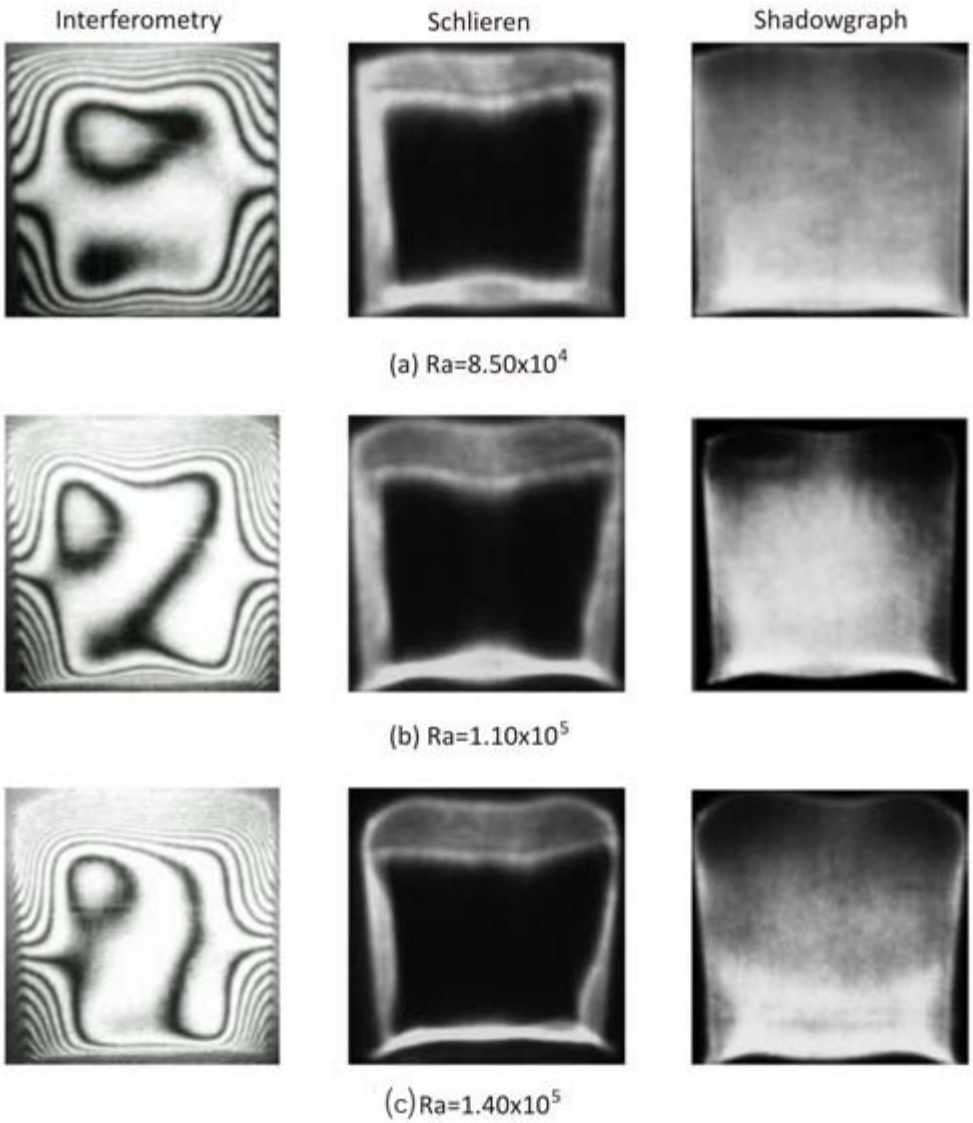

Figure 5.22: Interferograms, schlieren and shadowgraph images for the higher range of Rayleigh numbers in air.

At $Ra = 8.5 \times 10^4$, the interferogram shows nearly straight dense fringes parallel to the horizontal walls. These are indicative of near-parallel flow near the hot and the cold walls. The flow turns at the corners, leading further to fringe curvature and separation. The flow field is symmetric about the centerline of the cavity. These trends are well-reproduced by schlieren and shadowgraph images.

The movement of the fluid medium in the cavity cross-section has the shape of a roll. The roll size can be determined directly from the optical images since the fringes as well as the intensity fields should turn along at corners with the local velocity vector. The roll sizes of Figure 5.22 have been compared in Table 3, and are found to be quite close. The three experimental techniques reveal a reduction in the roll size with increasing Rayleigh number.

Table 3: A comparision of roll sizes of convection seen relative to the cavity height in the three optical techniques; effect of increasing Rayleigh Number.

Rayleigh Number	Interferometry	Schlieren	Shadowgraph
8.50×10^4	0.270	0.278	0.310
1.10×10^5	0.258	0.252	0.252
1.40×10^5	0.210	0.242	0.220

Previous Next

Thermal imaging of the test cell filled with water is reported in the following discussion. The vast difference in the properties of air and water leads to certain difficulties in temperature measurement in a water-filled cavity. Specifically, the following issues are to be noted:

1. Even for modest temperature differences, the equivalent Rayleigh numbers are very high. Consequently, the convective field reaches the unsteady, turbulent regime quite early.
2. The temperature drop per fringe shift is small in water. Thus the fringe density in interferograms is high, making data analysis difficult.
3. The sensitivity of the refractive index to temperature is high. Thus the deformation of the cavity size as seen on the screen is large and leads to ambiguity in data analysis.

In view of these complications, it is natural that shadowgraph should be best suited for temperature measurement in water. A comparison of interferometry, schlieren and shadowgraph for a temperature difference of $4K$ $(Ra = 2.5 \times 10^6)$ is presented in Figure 5.23. The optical images contain information that is path-integrated in the direction of propagation of light, but are functions of time. Figure 5.23 shows that the shadowgraph has the most well-defined intensity variation and is the easiest to analyze for the present experiment.

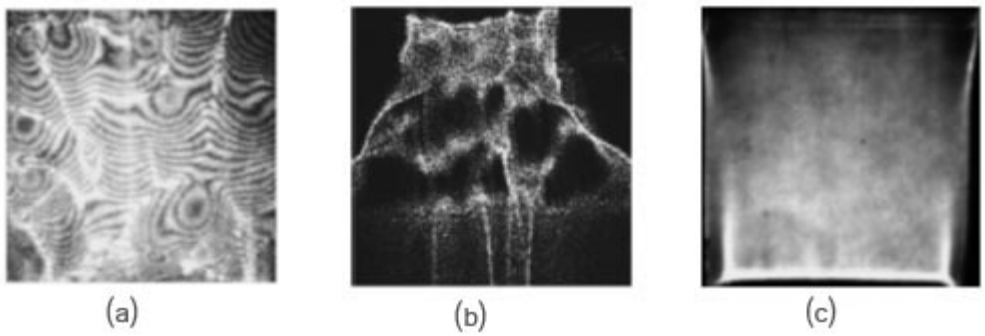

Figure 5.23: Comparsion of (a) interferogram, (b) schlieren and (c) shadowgraph for buoyant convection in a water-filled cavity at $Ra = 2.50 \times 10^6$

Previous Next

A comparison of shadowgraph images over a range of high Rayleigh numbers in water is shown in Figure 5.24. The light intensity variation shows the flow evolving from a boundary-layer type behavior at the lowest Rayleigh number towards large scale structures (namely, plumes) at the highest Rayleigh number. Beyond Ra = 5×10^6 the flow is unsteady as well. The images shown in Figure 5.24 have been time-averaged over a few seconds so that the dominant spatial features are captured.

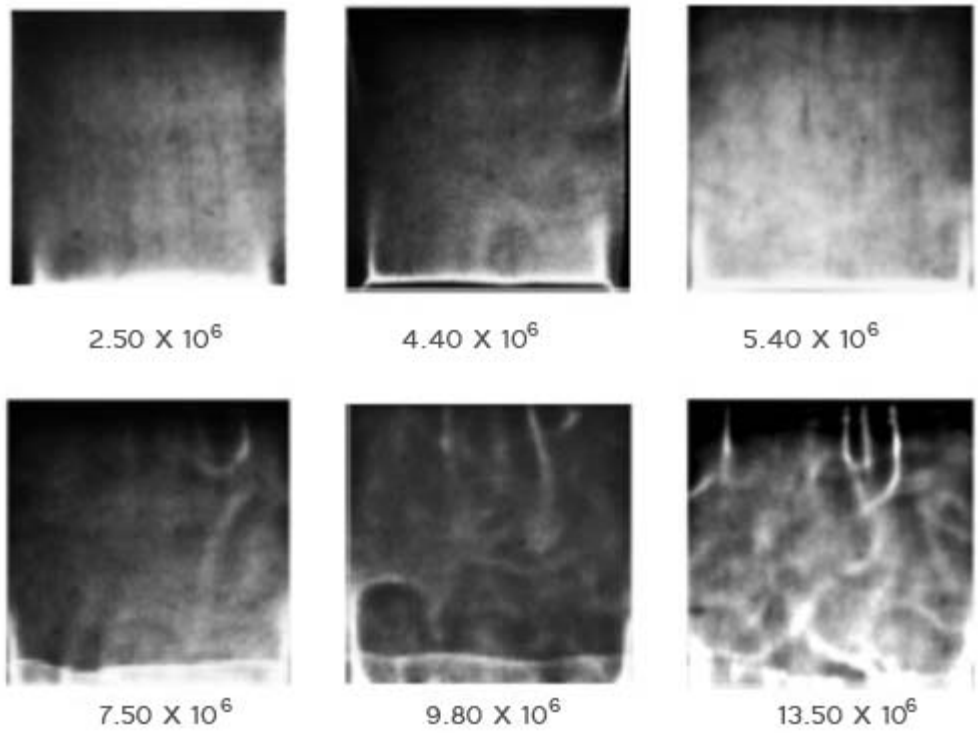

Figure 5.24: Shadowgraph images of the convective field with increasing Rayleigh number in water.

Previous Next

Convection in water at high Rayleigh numbers in the presence of an air-water interface is considered. A sequence of shadowgraph images recorded in the experiments is shown in Figure 5.25.

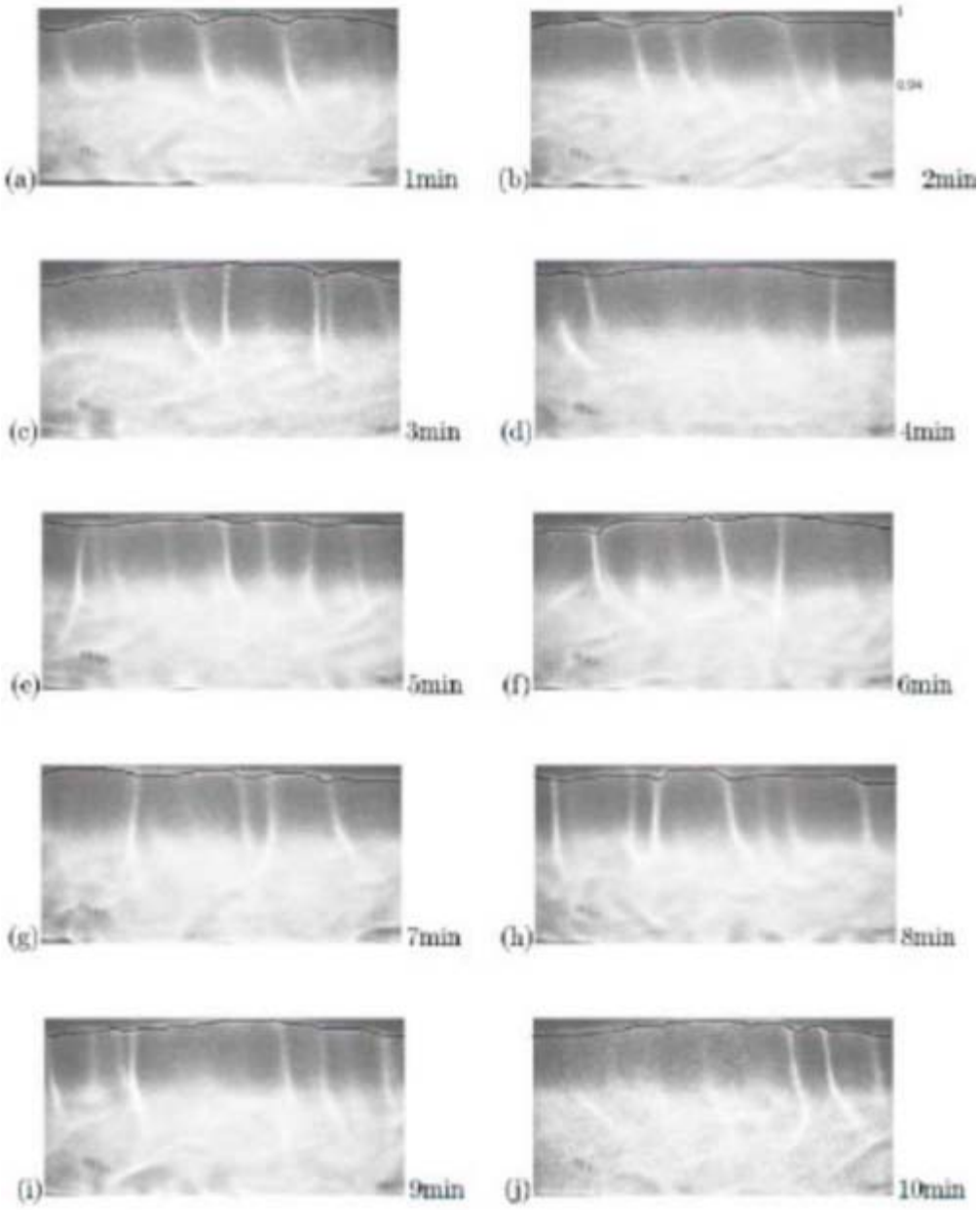

Figure 5.25: Shadowgraph images showing the deformed interfaces in a cavity half-filled with water, the best being air; Interfaces are emphsized in black.

Based on the above discussion, the following conclusions can be drawn.

1. In low temperature gradient experiments, all the three techniques correlate well with one another. Interferograms are limited by few fringes in air, and too many fringes in water. The shadowgraph image does not show sufficient contrast for analysis. In this respect, the schlieren technique is most amenable to data reduction.
2. In high gradient experiments, both schlieren and shadowgraph yield clear images. The interferograms are however corrupted by refraction errors. Schlieren and shadowgraph track the temporal response of the fluid medium in the form of the light intensity variation.
3. In high Rayleigh number experiments with water, the flow field is turbulent. Shadowgraph images are seen to be meaningful, as against interferograms and schlieren. The shadowgraph images reveal a considerable amount of physical information, including boundary-layers, plumes and time scales. It can be independently used to improve existing models of engineering turbulence.

Previous Next